Article

Not peer-reviewed version

Synthesis of a New Dinuclear Cu(I) Complex with Triazine Ligand and diphenylphosphine methane: X-ray Structure, Optical properties, DFT calculations and application in DSSC

Carlos A. Peñuelas , José J. Campos-Gaxiola * , Rody Soto-Rojo , Adriana Cruz-Enríquez , Edgar A. Reynoso-Soto , Valentín Miranda-Soto , Juventino J. García , Marcos Flores Alamo , Jesús Baldenebro-López , Daniel Glossman Mitnik

Posted Date: 4 September 2023

doi: 10.20944/preprints202309.0204.v1

Keywords: copper (I); triazine, phosphine, crystal structure, theoretical calculations, co-sensitized.

inorganics

MDPI

Article

Synthesis of a New Dinuclear Cu(I) Complex with Triazine Ligand and diphenylphosphine methane: X-ray Structure, Optical properties, DFT calculations and application in DSSC

Carlos A. Peñuelas [1], José J. Campos-Gaxiola [1,*], Rody Soto-Rojo [1], Adriana Cruz-Enríquez [1], Edgar A. Reynoso-Soto [2], Valentín Miranda-Soto [2], Juventino J. García [3], Marcos Flores-Álamo [3], Jesús Baldenebro-López [1] and Daniel Glossman-Mitnik [4]

[1] Facultad de Ingeniería Mochis, Universidad Autónoma de Sinaloa, Fuente de Poseidón y Prol. A. Flores S/N, C.P. 81223, C.U. Los Mochis, Sinaloa, México. e-mail: gaxiolajose@uas.edu.mx http://fim.uas.edu.mx/
[2] Tecnológico Nacional de México/Instituto Tecnológico de Tijuana/Centro de Graduados e Investigación en Química, Apartado Postal 1166, C.P. 22000, Tijuana, Baja California, México
[3] Facultad de Química, Universidad Nacional Autónoma de México, Cto. Exterior S/N, C.U., C.P. 04510, Ciudad de México
[4] Centro de Investigación en Materiales Avanzados, S. C., Miguel de Cervantes 120, Complejo Industrial Chihuahua, Chihuahua 31136, México
* Correspondence: gaxiolajose@uas.edu.mx

Abstract: A new copper(I) complex, $[Cu_2(L)_2dppm](PF_6)_2$ (**1**) [L = 3-(2-Pyridyl)-5,6-diphenyl-1,2,4-triazine and dppm: Bis(diphenylphosphino)methane] was prepared and characterized by IR, ^{1}H-NMR, ^{31}P-NMR spectroscopy, elemental and thermogravimetric analysis, and single-crystal X-ray diffraction technique. Complex **1** is a dinuclear compound, showing that L and dppm act as tridentate and bidentate chelating ligands, respectively. The two Cu(I) atoms exhibit a distorted tetrahedral coordination sphere embedded in N_3P environments. The supramolecular interactions in the solid-state structure are characterized by C–H···N, C–H···F, C-H···π and π···π intermolecular interactions that were analyzed by inspection of the Hirshfeld surface and fingerprint plots. Additionally, the complex was studied experimentally in solution by UV–Vis spectroscopy and cyclic voltammetry; also, theoretical studies with Time-Dependent Density Functional Theory (TD-DFT) were performed. Moreover, the optical and electrochemical properties have been studied, focusing on the band gap. Compound **1** has been used as a co-sensitizer in a dye-sensitized solar cell, showing good activity.

Keywords: copper (I); triazine, phosphine, crystal structure, theoretical calculations, co-sensitized.

Citation: To be added by editorial staff during production.

Academic Editor: Firstname Lastname

Received: date
Accepted: date
Published: date

1. Introduction

With the acceleration of industrialization, the demand for energy in today's society is increasing. Most of the global electricity production has been entrusted to fossil fuels, generating large quantities of carbon dioxide and being non-renewable. This greenhouse gas has now become a real threat to our global ecosystem [1, 2]. According to energy claims and consequent environmental concerns, solar energy-to-electricity conversion technologies (photovoltaics) constitute, at this instant, the central perspective for clean energy and have raised an accelerated development in renewable energy research [3,4]. Photovoltaic systems represent an essential solution because sunlight is the most abundant renewable resource [5,6], and photovoltaic devices can easily be integrated into buildings, providing high conversion efficiencies. In photovoltaic technology, particularly interesting are the so-called Dye-Sensitized Solar Cells (DSSCs), first described by Grätzel and O'Regan in 1991 [7]. There are two types of these devices based on a sensitizer:

organic dyes (purely organic compound) [8] and inorganic dyes (organometallic o coordination complex [9,10]. The organic compound or coordination complex in DSSCs is responsible for light recollection and electron transfer into the conduction band (CB) of a semiconductor electrode (typically TiO_2), to which it is chemically bonded [11]. The performance of the solar device depends further on the composition of the redox couple and the electrolyte and, most crucially, the dye properties [12]. Metal complexes have inherent advantages over organic photosensitizers as they are likely to exhibit higher thermal and photochemical stability. In this context, ruthenium (II) complexes such as N719 and N3 have received particular attention because of their fascinating properties and potential applications [13,14]. Over the past two decades, much effort has been spent optimizing these components to improve the DSSCs' overall efficiency [15,16]. Record efficiencies overcoming 11.9-20% [17,18] were obtained with the dye N719, often employed as a term of comparison in studies describing novel dyes for DSSCs.

Nevertheless, using ruthenium complexes as photosensitizers has a significant, potentially critical disadvantage. Ruthenium is present in the Earth's crust in low abundance (ca. 0.001 ppm)[19] and is expensive, raising questions about the technology's sustainability and commercial viability. Consequently, much effort has been invested in the search for photosensitizers based on other metal centers, which would be more sustainable and lower cost [19, 20]. The strong, appealing possibility of using costless and nontoxic metals, such as copper or zinc, as substitutes for the abovementioned more expensive ruthenium(II) complexes has stimulated further research in this field [10].

Copper is abundant in the Earth's crust (ca. 50 ppm)[19], and copper(I) centers possess a d^{10} electron configuration and a favored coordination number of four [21]. Complexes with two ligands containing 2,2′ -bipyridine or 1,10-phenanthroline metal-binding domains include similar photophysical properties to those of ruthenium(II) sensitizers. These attributes have stimulated the use of Cu(I) complexes for the preparation of diverse components in DSSCs, e.g., as hole-transporting materials (HTM) [22], redox mediators [23], and dyes [24].

Since the discovery by Sauvage and coworkers [25], a series of homoleptic copper(I) complexes of the type $[Cu(N\hat{}N)_2]^+$ with bpy ligands containing carboxylic acids as anchoring groups as dyes with large band-gap semiconductors (TiO_2 and ZnO) for DSSCs and reported a PCE which corresponds to 23.7% relative to a device regarding ruthenium(II) dye N719, significant progress has been made in the development of homoleptic $[Cu(N\hat{}N)_2]^+$ and heteroleptic $[Cu(N\hat{}N)(N\hat{}N)']^+$ or $[Cu(N\hat{}N)(P\hat{}P)]^+$ sensitizers (N^N = diimine chelating ligand; P^P = diphosphines chelating ligand) in dye-sensitized solar cells [26-28].

Our research groups reported previous theoretical and experimental studies of photophysical and electrochemical properties of heteroleptic Cu(I) complexes carrying sterically demanding tri- phenylphosphine (PPh_3) as ancillary ligand and either cis-(±)-2,4,5-tris(2-pyridyl)imidazoline or 2,4,6-tris(2-pyridyl)triazine or pyridine-2,5-dicarboxylic acid as anchoring ligand and their performance as co-sensitizer in DSSCs, achieving a FF ranging from 27.9% to 57.9%, efficiency (0.50%-2.92%) and η_{rel} to N719 (30.5-63.6%) [29, 30]. In this paper, we document the molecular and crystal structures of one novel dinuclear complex of composition $[Cu_2(L)_2dppm](PF_6)_2$ (1) [L = 3-(2-Pyridyl)-5,6 di phe-nyl-1,2,4-triazine and dppm: Bis(diphenylphosphino)methane] see Scheme 1. The compound exhibits interesting optical and electrochemical properties, which were evaluated in solution by UV–Vis spectroscopy and cyclic voltammetry and analyzed further by quantum chemical calculations. In addition, their efficiency as co-sensitizers in DSSCs was assessed.

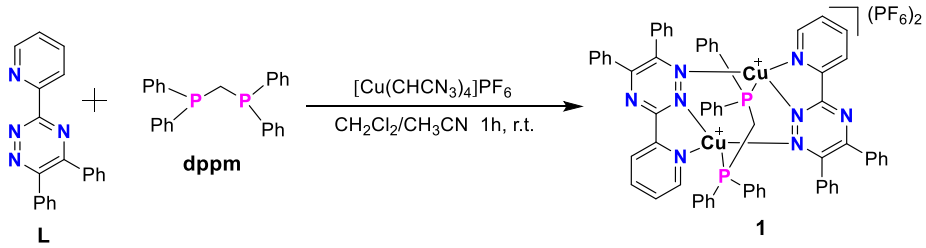

Scheme 1. Synthetic route for complex **1**.

2. Results and Discussion

Combination of 3-(2-Pyridyl)-5,6-diphenyl-1,2,4-triazine (L) and Bis(diphenylphosphino)methane (dppm) with $Cu(MeCN)_4PF_6$ provide a dinuclear Cu(I) complex of composition $[Cu_2(L)_2dppm](PF_6)_2$ (**1**). The phosphine ligands play a crucial role in stabilizing the molecular structure [31]. The compound was characterized by elemental analysis; IR, ^1H NMR, ^{31}P NMR (Figures S1-S3, in Supplementary Materials) and UV-Vis spectroscopy; thermogravimetric analysis (TGA) and single crystal X-ray diffraction (scXRD) analysis. In addition, the electrochemical properties of the compound were studied by cyclovoltammetry.

2.1. IR and NMR analysis

The IR spectrum of the title compound is in good agreement with the results of the X-ray structure analyses. The spectrum exhibits characteristic C-H stretching vibrations of the aromatic rings in the range of 3055-3050 $cm^{-1;\ the}$ stretching vibration of the $C{=}N_{imino}$ groups ($C{=}N_{triazine}$ 1600 cm^{-1} and $C{=}N_{py}$ 1511 cm^{-1}), which are shifted to higher frequencies (~ 15 cm^{-1}) in comparison with free L due to the formation of the N→Cu bond (see Table 1 and Figure S1). The signal for the C=C stretching bands of the pyridyl and phenyl groups appear at 1481-1436 cm^{-1}. The band around 1436 cm^{-1} is typical for $P\text{-}C_{Ar}$ vibration of the phosphine ligand, and other bands in the 1000 and 500 cm-1 region are attributed to out-of-plane bending modes for the C-H, C-C, and C-N bonds. Complex **1** exhibit also exhibits a band corresponding to the asymmetric stretching vibration of the PF_6^- group at 838 cm^{-1}. [32-34].

Table 1. Characteristic absorptions (cm^{-1}) in the IR spectra of ligands L, ppm, and complex $[Cu_2(L)_2dppm](PF_6)_2$.*

Compound	*ν* (C-H)	*ν* ($C{=}N_{imino}$)	*ν* (C=C)	*ν* (P-C)	*ν* (P-F)
L	3055 (w)	1579(m) 1502 (s)	1483 (m)	–	–
dppm	3050 (w)	–	1581(w) 1479 (m)	1429 (m)	–
$[Cu_2(L)_2dppm](PF_6)_2$	3054 (w)	1600 (m), 1511 (s)	1481 (m)	1436 (m)	838 (s)

* w = weak, m = medium, s = strong.

The ^1H NMR spectrum of the title complex (Figure S2, Supplementary material) displays slightly broadened resonances for the hydrogen atoms of coordinated L and dppm. The spectrum shows five sets of signals in the region 8.80-7.31 ppm that integrate for the 48 aromatic hydrogen atoms assigned to the L and dppm ligands. The two aliphatic hydrogens in the dppm appear at 3.93 ppm as a triplet (2H). The ^{31}P NMR spectrum of the

compound showed a broadened signal close to -7.42 ppm (see Figure S3), which was assigned to the dppm, in addition to a septet at -144.67 ppm arising from the PF_6^- anion [30,31,33].

2.2. X-ray Crystallography

Complex one was also characterized by single crystal X-ray diffraction analysis. The molecular structure with atom labeling is depicted in Figure 1. Selected bond lengths and bond angles are given in Table 2. Hydrogen bonding geometries are listed in Table S1(see Supplementary material).

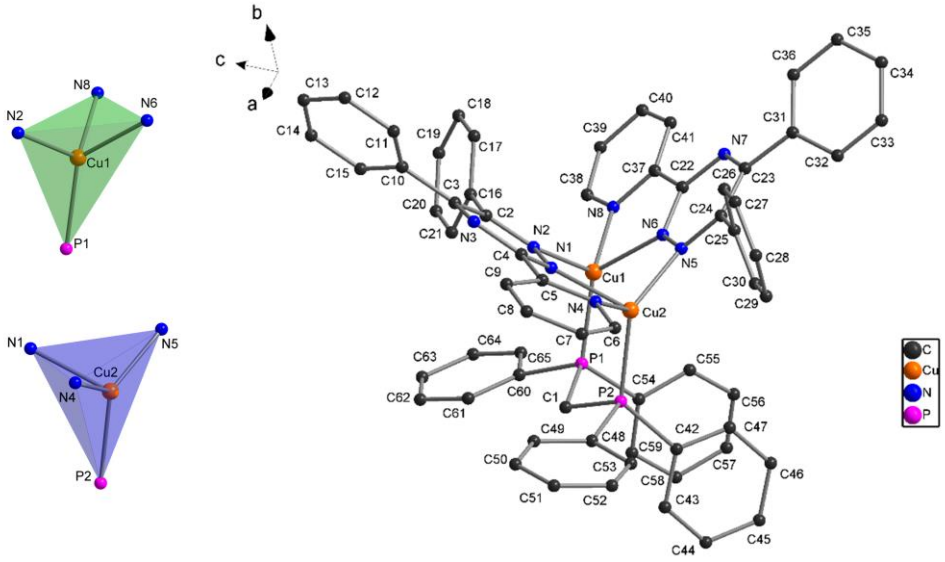

Figure 1. Perspective view of the molecular structure and metal coordination polyhedra for $[Cu_2(L)_2dppm]^+$ in the crystal structure of **1**. Hydrogen atoms and counterions have been omitted for clarity.

The crystallographic study revealed that $[Cu_2(L)_2dppm](PF_6)_2$ (**1**) crystallized in the monoclinic crystal system with space group $P2_1/c$. The asymmetric unit contains two copper(I) atoms as metal centers, two L ligands, one dppm molecule, and two PF_6^- anions. The central Cu(I) ions are embedded in a four-coordinate CuN_3P environment, resulting from coordination by the auxiliary phosphine ligand and triazine L ligands, which adopts the k^3-*N,N,N*-tridentate chelate coordination mode upon binding with the pyridyl nitrogen and two nitrogen atoms from the triazine group. Thus, two five-membered Cu-N-C-C-N, one six-membered Cu-N-N-Cu-N-N and one seven-membered Cu-N-N-Cu-P-C-P chelate rings are observed in the molecular structure (see, Figure S4) with Cu-N and Cu-P bond lengths in the range of 2.0160(3)–2.1360(3) Å and 2.1831(11)-2.2102(11) Å, respectively (Table 2). The bond angles at Cu(I) vary from 77.67(12) to 130.45(10)°, with the smallest value corresponding to the N-Cu-N angle in the five-membered chelate rings formed in the title compound. The largest bond angle [N(5)-Cu(2)-P(2)] is created with a sterically demanding dppm ligand in the seven-membered chelate ring. A comparison of the bite angle (N-Cu-N) of the triazine ligands with the bond angle calculated by DFT (M06/6-31G(d)+DZVP level) agrees well for Cu(1) and Cu(2) ions (see Table 2).

Table 2. Experimental (scXRD) and calculated (M06/6-31G(d)+DZVP) data of distances [Å] and angles [°] relevant to the coordination geometries of copper(I) atoms in complex.

Distances (Å) and angles (°)	Experimental	DFT	Δd / Δ∠
Cu(1)-N(8)	2.047(3)	2.094	0.0470
Cu(1)-N(2)	2.063(3)	2.111	0.0480
Cu(1)-N(6)	2.072(3)	2.169	0.0970
Cu(1)-P(1)	2.183(11)	2.222	0.0389
Cu(2)-N(5)	2.016(3)	2.062	0.0460
Cu(2)-N(4)	2.101(3)	2.132	0.0310
Cu(2)-N(1)	2.136(3)	2.163	0.0270
Cu(2)-P(2)	2.210(11)	2.224	0.0138
N(8)-Cu(1)-N(2)	111.85(13)	112.26	0.41
N(8)-Cu(1)-N(6)	79.00(13)	77.07	1.92
N(2)-Cu(1)-N(6)	95.50(13)	94.65	0.84
N(8)-Cu(1)-P(1)	129.33(10)	130.13	0.80
N(2)-Cu(1)-P(1)	108.25(9)	112.30	4.05
N(6)-Cu(1)-P(1)	126.45(9)	119.92	6.52
N(5)-Cu(2)-N(4)	120.54(13)	117.2	3.30
N(5)-Cu(2)-N(1)	96.31(12)	95.53	0.78
N(4)-Cu(2)-N(1)	77.67(12)	76.12	1.54
N(5)-Cu(2)-P(2)	130.45(10)	129.22	1.22
N(4)-Cu(2)-P(2)	106.72(9)	111.54	4.81
N(1)-Cu(2)-P(2)	108.05(9)	109.19	1.14

The main distortion of the resulting tetrahedral coordination geometry originates from the small N(1)-Cu(1)-N(4) and N(6)-Cu(2)-N(8) bite angles of the chelating triazine ligands [77.67(12)° and 79.00(13)°, respectively]. The distortion of the tetrahedral geometry around the Cu(I) centers can also be seen from the dihedral angle formed between the two five-membered chelate rings, 74.18° (Figure 1). The coordination geometry is best described as distorted trigonal pyramidal, as indicated by the τ_4-values of 0.74 for Cu(1) and 0.77 for Cu(2) [35]. The geometries are similar to that reported previously for $[Cu2(N^N)_2(dppm)_2](BF4)_2$ (N^N=2-(2-tert-butyl-tetrazol-5-yl)pyridine) [36], $[\{Cu(pypzH)\}_2(\mu\text{-}dppm)_2](ClO_4)_2$ (pypzH=3-(2′-pyridyl)pyrazole) [37] and $[Cu(N^N)(PPh_3)_2]NO_3$ (N^N = 5,6-diphenyl-3-pyridin-2-yl-[1,2,4]triazine) [38]. In **1**, the intramolecular Cu(1)···Cu(2) distance is 3.217 Å; this value is longer than the sum of van der Waals radii of Cu (2.8 Å), which does not favor metal-metal interaction. In this complex, two face-to-face intramolecular π-stacking interactions stabilize the structure further (Figure S5). The first π-contact is within one dppm ligand (angle between ring planes = 12.4°, centroid···ring plane = 3.62 Å, distance between ring centroids = 3.68 Å). The second is between the phenyl ring of the dppm ligand and the pyridine ring (angle between ring planes = 16.1°, centroid···ring plane = 3.69 Å, distance between ring centroids = 3.80 Å) [39, 40].

A close inspection of the crystal structure of the complex reveals a 3D hydrogen bond network, in which two different dimeric units formed through C-H···π and π···π contacts [39,41] between two $[Cu_2(L)_2dppm]^+$ cations (Figure S6 and S7). The crystal structure is stabilized by a series of additional C–H···N, C-H···F, C-H···π and π···π interactions between the components of the complex. The details of these supramolecular interactions are

summarized in Table S1. All distances and angles are within the range found for previously reported structures [29,30,33, 42, 43].

2.3. Hirshfeld Surface Analysis.

Hirshfeld surface analysis detects different intermolecular interactions in crystal packing [44,45]. For this purpose, a crystallographic information file (CIF) was used as the input to generate the Hirshfeld surfaces and fingerprint plots using the CrystalExplorer program. The red-blue-white color scheme is utilized for quantifying the intermolecular interactions and provides a resource to analyze the zones of strong donor–acceptor interactions [44]. The Hirshfeld surface of the title complex is mapped over the d_{norm} (0.5 to 1.5), curvedness, and shape index (Figure 2). The plot reports the distances to the closest atom inside the surface (di) and to the closest atom outside the surface (de). The differences in the plots reveal variations in the packing modes of the structures. Intermolecular π···π interactions between neighboring molecules in the structures of molecular crystals give rise to patches in the curvedness map [46]. The curvedness plots (-4.0 to +4.0) of the complex show only slightly flattened surface patches above either side of the aromatic rings from the L ligand, indicating that the π···π contacts are relatively weak and significantly face-to-face displaced (Figure 2b). Maps of the shape index are more sensitive to subtle changes in the electron density surrounding the molecules [45,46]. The shape index curve exhibits complementary red (pit) - blue (bump) that correspond to the negative and positive surface property value, respectively, the former representing the location of an acceptor atom and the latter pointing towards a donor atom and are involved in C–H···N, C-H···F, C-H···π and π···π interactions, in agreement with the observations in the scXRD section (Figure 2c).

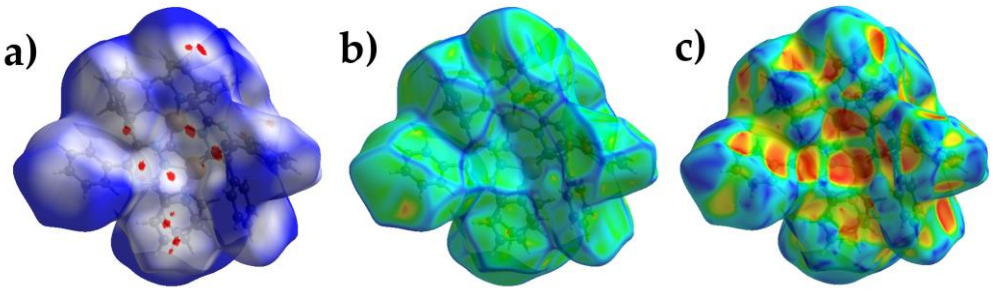

Figure 2. Hirshfeld surface for the title complex mapped with d_{norm} (a), curvedness (b), and shape index (c).

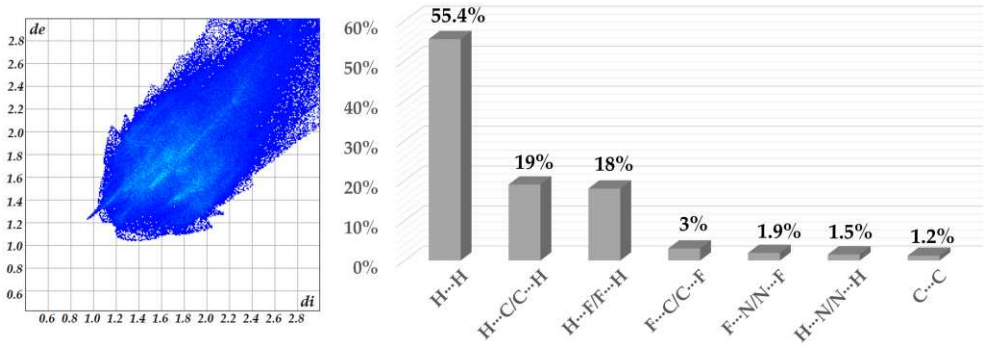

Figure 3. 2-D full fingerprint plot and percentage contributions of the Hirshfeld surface area for Complex

The dominant interactions observed in complex **1** are H···H (55.4%), H···C (19%), H···F (18%), and C···F (%) which appear as red spots on the d_{norm} surface in Figure 2a.

Furthermore, the intermolecular interactions in the complex are represented in the 2D fingerprint plots shown in Figures 3 and S8, respectively. The fingerprints around 1.6-1.8 (di, de) vary from a blue tone to a slightly green color and are associated with the C···C contacts from π···π interactions [47,48]. The H···F/F···H and H···N/N···H interactions appear as distinct spikes in the fingerprint plot and comprise 18% and 1.5%, respectively, of the total Hirshfeld surface for complex **1** (Figures 3 and S8). The more dispersed zones in blue color correspond mainly to H···H (55.4%) van der Waals contacts. The significant contribution of H···H contacts indicates that aside from the hydrogen bonding interactions, van der Waals contacts are relevant for the molecular packing of the components in the crystal structure.

2.4. Analsisis DFT and UV–Vis

The complex's molecular structures and electronic properties were calculated using DFT [49,50] and TD-DFT methods [51,52]. The calculations were carried out using the M06 hybrid-meta-GGA function in combination with the base sets 6–31G(d) (for C, H, N, and P atoms) and DZVP (Cu atom) with an IEF- PCM in ethanol [53-55]. X-ray crystallographic analysis determined The ground state geometries from the experimental structure. Notably, the deviations between the simulated molecular structure in solution and the solid-state structure are less than 0.097 Å and 6.52°, respectively (see Table 2).

It is well known that frontier molecular orbital analysis is a potential tool for studying molecular electronic charge mobility, the chemical reactivity, kinetic stability of molecules, and electronic transitions in the molecules. The energy gap between the highest occupied molecular orbital (HOMO) and the lowest unoccupied molecular orbital (LUMO) is an essential parameter for determining the photophysical and electrical properties of organic and inorganic materials [29,30,33].

Considering that the electronic excitations crucial for the optical absorption processes are HOMO→LUMO transitions, it is important to introduce the separate states of charge with the HOMO located in a donor unit and the LUMO in an acceptor unit. The isodensity plots of the frontier molecular orbitals (FMO) for the asymmetric unit of $[Cu_2(L)_2dppm]^{2+}$ at the M06/6-31G(d) + DZVP level of theory of calculation show charge transfer (HOMO→LUMO) over the entire π-system of the compound and the copper metal center. The energy of the highest occupied molecular orbital (E_{HOMO}) is -6.656 eV, and the energy of the lowest unoccupied molecular orbital (E_{LUMO}) is -3.034 eV, giving $\Delta E_{(LUMO-HOMO)}$ = 3.623 eV (Figure 4). As shown in Figure 4 and S9, the HOMO orbital is mainly concentrated in the copper metal centers and the two phosphorus atoms, while the LUMO electron density is mainly distributed in the L ligands. Furthermore, Figure S7 shows that HOMO - 4, HOMO – 5, and HOMO - 6 orbitals are distributed over the L and dppm ligands, while LUMO + 1 and LUMO + orbitals are distributed only in the triazine ligands. The HOMO and LUMO energy levels of $[Cu_2(L)_2dppm]^{2+}$ are shown in Figure 4. It shows that the energy levels of the complex are appropriate for the DSSC system containing TiO_2 because the LUMO levels lay above the conduction band of the TiO_2 semiconductor (−4.40 eV), indicating efficient electron injection and the HOMO energy levels lay below that of the I^-/I_3^- redox electrolyte (−4.60 eV) which can be further improved (about −0.3 V) by adding additives such as 4-tert-butyl pyridine (TBP) to the I^-/I_3^- redox electrolyte, providing sufficient driving force for dye regeneration [56-57].

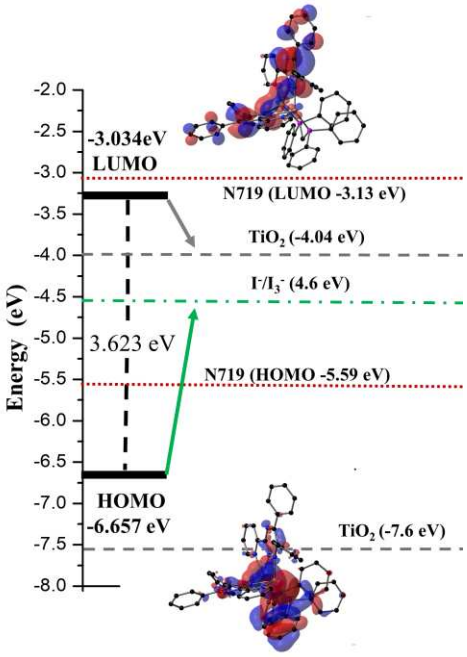

Figure 4. A plot of the molecular orbitals involved in the lowest-lying electronic absorption transitions in the complex.

The experimental and calculated UV-Vis absorption spectra of the title compound are shown in Fig. 5. The experimental spectrum was measured from a 2.0 x 10^{-5} M solution in EtOH at room temperature. The oscillator strength (f) is a parameter that quantifies the probability of electron transitions and is calculated based on TD-DFT/M06/6-31G(d) + DZVP level of theory. The results of the TD-DFT calculation indicate three major transitions for the complex $[Cu_2(L)_2dppm]^{2+}$ (Figures 5 and S10; Table 4), of which the most intense band at 446 nm (f = 0.0922) is due to the HOMO→LUMO transition having MLCT/XLCT/LLCT character. This excitation is consistent with the experimental spectrum's broad band centered at 410 nm (ε= 13150 M^{-1} cm^{-1}, see Figures 5 and Table 4).

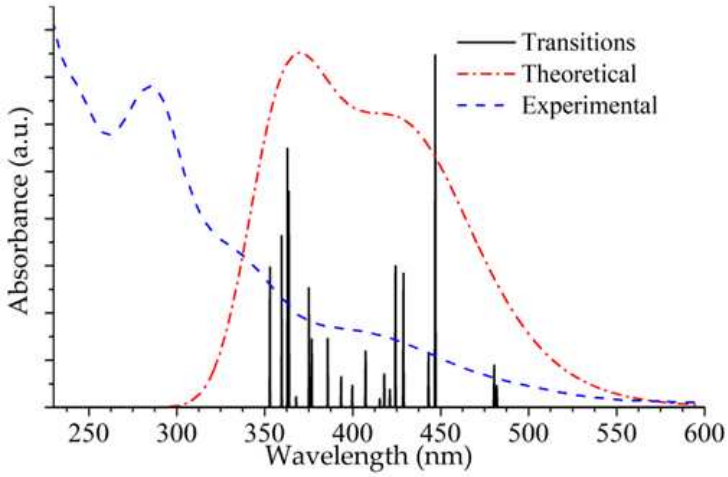

Figure 5. Experimental and calculated absorption spectra of $[Cu_2(L)_2dppm](PF_6)_2$.

The calculated spectrum displays two additional bands at 363 nm (f = 0.0565) and 359 nm (f = 0.0449), which are assigned to HOMO-3→LUMO+3/HOMO-6→LUMO and HOMO-10→LUMO/HOMO-6→LUMO transitions, respectively. These transitions imply that intramolecular charge transfer takes place [29,30,58]; the band at 363 nm can be related to the broad experimental absorption band found at 338 nm (ε = 26700 M^{-1} cm^{-1}, Figures 5 and S10) and has LLCT character. The experimental band centered at 286 nm (ε = 56700 M^{-1} cm^{-1}) was assigned to π→π* transitions having LLCT character. A detailed assignment of the TD-DFT calculations in terms of FMO is included in Table 4.

Table 4. Principal electronic excited states calculated by time-dependent density functional theory (TD-DFT) at M06/6-31G(d)+DZVP level of calculation, together with the experimental values.*

λ_{DFT} (nm) E(eV))	λ_{Exp} (nm)	Oscillator strength	Transition (CI Coef.)	Character
446(2.77)	410	0.0922	HOMO→LUMO (41%) HOMO-2→LUMO (25%)	MLCT/XLCT/LLCT
428(2.89)		0.035	HOMO→LUMO+1(29%) HOMO-2→LUMO+1(21%)	MLCT/XLCT/LLCT
424(2.92)		0.037	HOMO-1→LUMO+1(29%)	MLCT/XLCT/LLCT
363(2.41)	338	0.0565	HOMO-3→LUMO+3 (34%) HOMO-6→LUMO (21%)	LLCT
375(3.31)		0.0313	HOMO-6→LUMO (26%)	LLCT
359(3.45)	286	0.0449	HOMO-10→LUMO (20%) HOMO-6→LUMO (18%)	LLCT
352(3.51)		0.0367	HOMO-5→LUMO+1 (36%) HOMO-4→LUMO (21%)	MLCT/XLCT/LLCT

*Metal-to-ligand charge transfer (MLCT); Ligand-to-ligand charge transfer (LLCT); Phosphine-to-ligand charge transfer (XLCT).

2.4. Electrochemical Properties

The electrochemical properties of the dinuclear complex were investigated at 298 K for solutions in acetonitrile by cyclic voltammetry (CV) using 0.1 M of tetrabutylammonium hexafluorophosphate (NBu_4PF_6) as a supporting electrolyte. The analyzed data are found in Table 3, and the CV is shown in Figure S11. The complex showed irreversible oxidation and reduction waves. The first oxidation (E_{pa} = 0.97 V) corresponds to the Cu(I)/Cu(II) redox couple with significant P^P character, indicating stronger structural rigidity [30,59]. The compound shows a second irreversible oxidation wave (E_{ox} = 1.15 V) assigned to oxidation of the second copper center, revealing the expected electronic communication between the two metals [59]. The oxidation potential (+0.97 V and +1.15 V) is within the range reported for copper(I)-pyridyl complexes [29,30,59,60]. The first reduction event (E_{red1} = -0.81 V) is centered on the pyridine ring of the L ligand; a second reduction wave at −1.96 V is assigned to a second reduction of the L ligand [30,59]. Based on the reduction potentials, the HOMO and LUMO energy levels were calculated using the equation 1 [61,62]:

$$E_{HOMO} \text{ (or } E_{LUMO}) = -4.8 - [(E_{peak\ potential} - E_{1/2} \text{ (ferrocene)}] \quad (1)$$

Where, $E_{peak\ potential}$ corresponds to the maximum and minimum peak potential and $E_{1/2}$ is the half-wave potential of ferrocene (0.42 V), which was used as a reference. The resulting value for the HOMO orbital (-5.53 eV) is in good agreement with the values obtained by the DFT calculations with -6.65 eV. Due to the irreversibility of the redox process, it was not possible to obtain a good approach for the LUMO value.

Table 5. Selected electrochemical data of the $[Cu_2(L)_2dppm](PF_6)_2$ complex in acetonitrile.*

	E_{ox} [V]	E_{red} [V]	E_{HOMO} [eV]	E_{LUMO} [eV]	$E_{HOMO/DFT}$ [eV]	$E_{LUMO/DFT}$ [eV]	Δ_E [eV]	$\Delta_{E/DFT}$ [eV]
Complex	1.15	-1.61	-5.53	-2.77	-6.657	-3.034	2.76	3.623

* The CV was recorded in acetonitrile solution for complex (5×10^{-3} M) with 0.1 M of NBu_4PF_6 (T = 298 K, scan rate = 25 mV s^{-1}), Δ_E [eV] = E_{LUMO}-E_{HOMO}.

2.5. TGA analysis

To investigate the thermal stability of compound **1**, thermogravimetric analysis (TGA) was performed over the temperature range of 30-800 °C under N_2 atmosphere for a crystalline sample with a heating rate of 20 °C min^{-1} (see Figure 6). The TGA graph indicates the first weight loss (found 10.0%; theoretical,10.2%), in the 300–350 °C range, attributed to the loss of one PF_6 ion. The second step in the temperature range of 350 to 450 °C corresponds to the loss of two L ligands, one dppm molecule, and one PF_6 ion. The observed weight loss of 80.3% agrees with the calculated value (80.9%). The residual framework starts to decompose beyond 450 °C with a series of complicated weight losses and does not stop until heating ends at 800 °C.

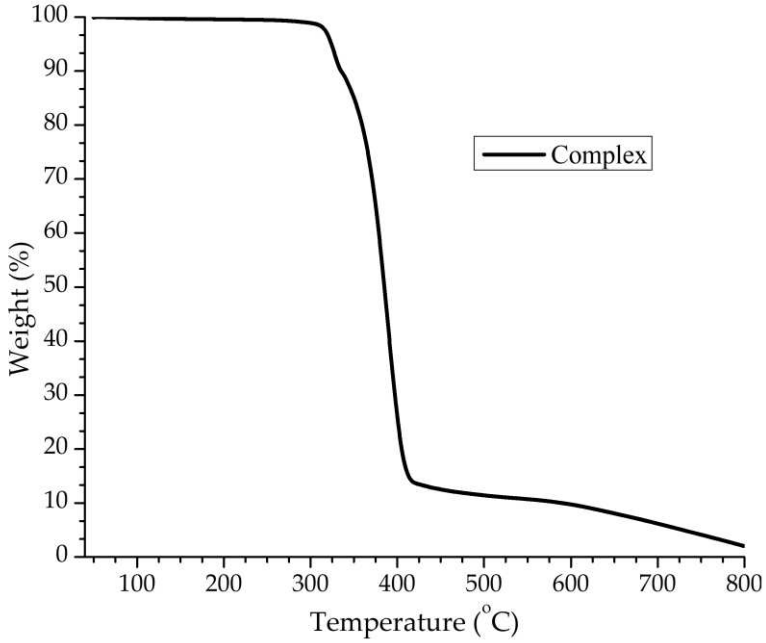

Figure 6. TGA curve of the complex **1**.

2.6. Application in DSSCs

UV-Vis absorption spectra of the free ligand L, complex **1**, and N719 were measured in ethanol at room temperature (Figure S10). The complex showed a metal-to-ligand

charge transfer (MLCT) absorption band between 350 and 550 nm. Compared to the commercially available N719 ruthenium complex, which absorbs in the 330 to 600 nm range [63], the complex could achieve absorption in low wavelength when used as a co-sensitizer in DSSCs. To evidence this hypothesis, two DSSC devices were developed; the first was sensitized with N719 alone and was used as a control, and the second was co-sensitized with a 1:1 mixture of complex **1** and N719. Notably, the amount of N719 used in the co-sensitized device was only half that of the control DSSC.

The current-voltage (J–V) characteristics of the DSSC device based on the N719 and complex/N719 photoanodes are shown in Figure 7, and the efficiencies of the corresponding cells are summarized in Table 6. Under standard global AM1.5 solar irradiation conditions, the electrode performance (η_{rel}) of the complex/N719/TiO_2 co-sensitized solar cell decreased by 7.63%, representing an acceptable value because the amount of N719 was lower. These results suggest that the co-sensitization of TiO_2/N719 photoelectrodes with the Cu(I) complex is an option to reduce the amount of N719 dye, putting costs with a minor impact on the efficiency of DSSCs.

Table 6. J-V performance of DSSCs based on different photoelectrodes.

Dyes	j_{sc} (mA/cm^2)	Voc (V)	ff (%)	η (%)	$\eta_{Relative}$ (%)
[a]Complex/N719	5.095	0.757	52.7	2.03	92.27
N719	6.030	0.770	47.3	2.2	100

Jsc = short circuit current, VOC = open circuit potential, ff = fill factor, η = power conversion Efficiency. [a]The electrode based on the dye combinations 1/N719 contains only 50% of N719 compared to the control experiment with only N719.

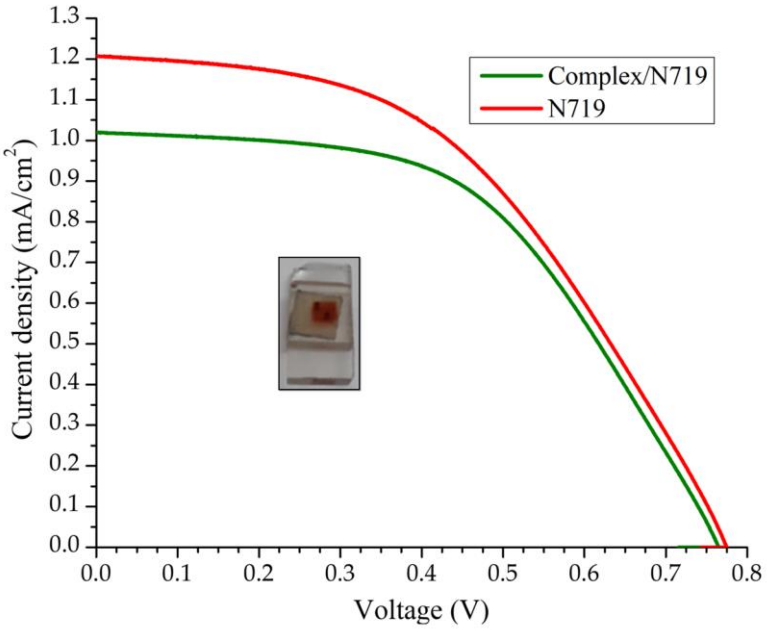

Figure 7. J–V curves for DSSCs of N719 and complex/N719. Inset: Photo of the DSSC device containing dye complex/N719.

3. Conclusions

A new dinuclear copper(I) compound based on the 3-(2-Pyridyl)-5,6-diphenyl-1,2,4-triazine as chelating ligand and auxiliary phosphine Bis(diphenylphosphino)methane was synthesized and characterized by elemental analysis, single crystal X-ray crystallography, and NMR, IR and UV-Vis spectroscopy. Electrochemical, spectroscopic, and computational studies were used to understand the electronic characteristics of the compound. Single crystal X-ray diffraction revealed that the complex possesses a distorted trigonal pyramidal geometry and a variety of supramolecular interactions, such as C-H···N, C-H···π and π···π that stabilize the crystalline structure. Comparison of experimental (SCXRD analysis) and calculated (DFT/M06/6-31G(d)+DZVP) bond lengths and bond angles showed excellent agreement with variations less than 0.097 Å and 6.52°, respectively. Complexes **1** displays a low-intensity band at 410 nm, corresponding to MLCT transitions, consistent with the theoretical calculation realized with EtOH. According to the voltammetry analysis, the complex shows irreversible oxidation processes, which constitutes a drawback for the regeneration of dyes within DSSC devices. Devices based on TiO_2/N719 and co-sensitized with the complex produce overall efficiencies of 92.27%, which is a bit lower than the reference device but employs only half the amount of the expensive and more toxic ruthenium dye (N719). These results are relevant for the future design of co-sensitizers for the fabrication of new DSSCs with significantly low cost and higher availability of the Earth-abundant copper-based precursors.

4. Materials and Methods

4.1. General

All chemicals, such as 3-(2-Pyridyl)-5,6-diphenyl-1,2,4-triazine (L) and Bis(diphenylphosphino)methane (dppm) and $[Cu(MeCN)_4]PF_6$ were purchased from Sigma-Aldrich and used as received without further purification. Dye N719 was purchased from *Solaronix*. Elemental analysis was performed on an Elementar Vario ELII instrument. IR spectra were obtained using a Bruker Alpha Tensor 27 Vertex Series spectrophotometer with KBr pellets in the 4000–500 cm-1 region. The ^{1}H and ^{31}P NMR spectra were determined with Bruker Advance III-400 spectrometer. Chemical shifts are reported in ppm and were referenced to residual solvent resonances. Uv-vis absorption spectra were recorded on a Shimadzu UV-1800 spectrophotometer. Electrochemical measurements were made using an electrochemistry workstation (Bio-Logic VMP-300 potentiostat/galvanostat) with platinum, silver wire, and $Ag/AgNO_3$ as working, counter, and reference electrodes, respectively. Substrates were dissolved in HPLC grade CH_3CN (ca. 8 × 10−5 M) containing 0.025 M tetrabutylammonium hexafluorophosphate $(nBu_4N)PF_6$ as supporting electrolyte. The scan rate was 20 mVs^{-1}. Thermogravimetric analyses were performed on a TA SDT Q600 apparatus in a range of 30-800 °C (10 °C min^{-1}) using nitrogen (50 mL min^{-1}) as a purge gas.

4.2. Preparation of $[Cu_2(L)_2dppm](PF_6)_2$ (1)

To a stirring solution of [3-(2-Pyridyl)-5,6-diphenyl-1,2,4-triazine)] (L) (40 mg, 0.12888 mmol) and bis(diphenylphosphino)methane (dppm) (25.10 mg, 0.06444 mmol) in 2 mL of a 1:1 (*v*/*v*) mixture of CH_2Cl_2 and CH_3CN, $[Cu(MeCN)_4]PF_6$ (48.04 mg, 0.06444 mmol) was added to obtain a dark red solution. The mixture was stirred throughout 2 h

at 30 °C. Red single-crystals were obtained by vapor diffusion of diethyl ether into the concentrated solution of **1** (yield: 85.98 mg, 76%). IR (KBr, cm^{-1}): 3054 (w), 1600 (w), 1511 (m), 1479 (w), 1436 (m), 1402 (m), 1373 (m), 1305 (w), 1282 (w), 1257 (w), 1186 (w), 1143 (w), 1099 (w), 1006 (w) , 838 (s), 771 (m), 740 (m), 698 (w), 607 (m), 557 (m), 520 (w) cm^{-1}. ^{1}H NMR (400 MHz, acetone-d_6, 30 °C) δ 8.80 (d, *J*=8 Hz, 2H, Ar-H), 8.17 (t, *J*=8.00 Hz, 2H, Ar-H), 7.64 (m, 4H, Ar-H), 7.52 (m, 14H, Ar-H), 7.34 (m, 25H, Ar-H), 3.93 (t, *J*=8 Hz, 2H, CH_2) ppm. ^{31}P NMR (162 MHz, acetone-d_6, 30 °C) δ -7.42 (s, Ar-P), -144.67 (hept, ^1J = 708.47 Hz, PF_6) ppm. UV–Vis (ethanol 2 x 10^{-5} mol dm^{-3}): λ (ε: M^{-1} cm^{-1}) 286 (56700), 338 (26700), 410 (13150) nm. Anal. Calc. (%) for $C_{65}H_{50}Cu_2F_{12}N_8P_4$: C, 54.90; H, 3.54; N, 7.88. Found (%): C, 54.63; H, 3.91; N, 7.93.

4.3. Crystallography

The single crystalline X-ray diffraction study of the title complex was determined at T = 130 K in an Oxford Diffraction Gemini "A" diffractometer equipped with a CCD detector and using Mo-Kα radiation (λ = 0.71073 Å) and an Oxford Instruments Cryojet ES-75 cooler. Unit cell parameters were calculated with a set of three runs of 15 frames each (1° in ω). The double pass scanning method was used to exclude noise [64]. The collected frames were integrated using an orientation matrix resolution of the narrower frame scans. The final cell constants were obtained by global refinement. Diffraction data were corrected for absorbance through an analytical-numerical absorption correction, which employed a multifaceted crystal model based on Laue symmetry expressions with equivalent reflections [65]. Structure resolution and refinement were performed with SHELXT-2014 [66] and SHELXL-2014 [67]. All non-hydrogen atoms were refined anisotropically. All hydrogen atoms were placed in positions calculated geometrically using the driving model. Hydrogen bonding interactions in the crystal lattice were determined with the MERCURY software package [68]. The figures were made with MERCURY [68] and DIAMOND [69].

1: $C_{65}H_{50}Cu_2F_{12}N_8P_4$, *MW* = 1422.09 g mol^{-1}, monoclinic, space group $P2_1/c$, a = 18.9916(9), b = 18.6701(9), c = 20.9494(5) Å, α = 90, β = 111.621(6), γ = 90°, V = 6905.5(6)Å^3, D_c = 1.368 g cm^{-3}, T = 130 K, Z = 4, μ(Mo$K\alpha$) = 0.785 mm^{-1}. Total 38,974 reflections, 16,247 unique (R_{int} = 0.0427). Refinement of 16,247 reflections (820 parameters) with $I > 2\sigma(I)$ coverged at final R_1 = 0.0587 (R_1 all data = 0.1131), wR_2 = 0.1280 (wR_2 all data = 0.1644), F(000) = 2888, *gof* = 1.059. CCDC 2278925.

4.4. Solar cell construction

Material for the manufacture of dye-sensitized solar cells was purchased from Solaronix, Switzerland. DSSCs sensitized with $[Cu_2(L)_2dppm](PF_6)_2$ (**1**) and 1:1 dye combination **1**/N719 and N719 were prepared, modifying the method of Grätzel [70,71]. To prepare the working electrodes, fluorine-doped tin oxide (FTO) glass plates (Solaronix TCO30-8, 3 mm thick) were washed in a consecutive ultrasonic bath in a 1% soap solution, distilled water, and ethanol (HPLC grade) for 10 min each. Finally, the electrodes were subjected to UV light (λ = 254 nm) for 10 minutes in a peroxide solution in deionized water (5%). Subsequently, with the Deep Coating method, a compact layer of TiO_2 was added to each FTO plate by immersion in a 40 mM $TiCl_4$ aqueous solution (70 °C for 30 min), after which they were washed with distilled water and ethanol. Next, the glass plates were sintered with TiO_2 at 450 °C for 30 min in a muffle (Thermolyne SCIENTIFIC FB1410M); they were allowed to cool to room temperature and washed with ethanol. Therefore, with the Screen Print method, mesoporous TiO_2 was deposited on each FTO glass (0.2 cm^2), and finally, the sintering process was repeated. Once cooled, a second Dip Coating treatment was performed, followed by a 1-hour treatment with UV radiation (λ = 254 nm). In 0.3 mM

solutions of complex or N719 in a mixture of solvent CH_3CN/tert-butanol (50:50% v/v), the electrodes were immersed for 12 h in the dark. In co-sensitization, the electrodes were first immersed with the complex for 6 h in 0.3 mM solutions in a mixture of acetonitrile/tert-butanol (50:50% v/v). They were immersed for another 6 h in N719 under the same conditions. Finally, with ethanol, the electrodes were rinsed and dried. For the elaboration of the counter electrodes, FTO plates with 0.5 mm diameter holes on the edge of the driver's side were used. The FTO glasses were cleaned with the abovementioned procedure for the working electrodes. Accordingly, the platinum layer was deposited by screen printing on the entire surface of the FTO glass, followed by drying at 120 °C for 10 min. The plates were then immediately immersed for 1 min in a 10 mM H_2PtCl_4 solution in isopropanol and dried at 120 °C for 5 min. Finally, a heat treatment was applied at 400 °C (heating rate 1.2 °C/min) for 15 min, followed by cooling to 100 °C at a rate of 10 °C/min.

The working and counter-electrodes were joined by a thermoplastic (Meltonix 1170-25 DuPont Surlyn) of 60 μm thickness (treatment at 110 °C for ~5 min in an oven). Finally, an electrolyte composed of 0.05 M I_2, 0.1 M LiI, 0.5 M 4-tert-butylpyridine, and 0.6 M tetrabutylammonium iodide dissolved in a mixture of acetonitrile and 3-methoxypropionitrile (50:50% v/v) was introduced into the DSSCs. The remaining air was removed by vacuum treatment.

With a potentiostat/galvanostat (Bio-Logic VMP-300) and an AM 1.5 light source solar simulator (Oriel LCS-100), the performance of the DSSCs was measured by lateral irradiation of the DSSC anode. The incident light intensity was 100 mW cm^{-2} (1 sun), calibrated using a reference Silicon solar cell.

4.5. Computational detail

Hirshfeld surface analysis and complex fingerprint plots were performed from the Crystallographic Information Files (CIF) using *CrystalExplorer* 17 [72]. The Hirshfeld surface was mapped in the range 0.5 to +1.5 for d_{norm}, -4 to 0.4 in Curvedness, and Shape Index -1 to 1.

DFT analysis [49,50] for the complex was performed with the *Gaussian 09* package [73] and processed with the GaussView and Swizard software [74,75]. Starting from the monocrystalline structure by diffraction, the minimum energy structures were determined by frequency calculations (without imaginary frequencies). Using time-dependent density functional theory (TD-DFT), the transitions between the different molecular orbitals [51,52] were determined using the M06 hybrid-meta-GGA functional [53] in combination with the 6-31G(d) base sets [54] for the C, H, N and P atoms and DZVP [55] for the Cu atom. The effects of a solvated environment were estimated with the integral equation formalism for the continuum polarizable model (IEF-PCM) and the implementation of the out-of-equilibrium solvation model [76,77]. The solvent used for this analysis was ethanol.

Supplementary Materials: The following supporting information can be downloaded at: www.mdpi.com/xxx/s1: Figures S1, S2, and S3, IR, ^{1}H-NMR and ^{31}P-NMR spectra of **1**; Table S1, geometries of intermolecular hydrogen bonds and π···π contacts in complex **1**. Figure S4, perspective views of $[Cu2(L)2dppm]^+$ in the crystal structure of 1, showing a) two five-membered Cu-N-C-C-N, b) one six-membered Cu-N-N-Cu-N-N and c) one seven-membered Cu-N-N-Cu-P-C-P chelate rings; Figure S5, intramolecular π···π interactions in the crystal structure of **1**; Figure S6, intermolecular C-H···π and π-stacking interactions between pair of $[Cu2(L)2dppm]^+$ cations; Figure S7, perspective view of the three-dimensional (3D) hydrogen-bonded network in the crystal structure of complex **1**, formed through C-H···N, C-H···F, C-H···π and π···π interactions; Figure S8, percentages of intermolecular interactions in the fingerprint plot for complex **1**; Figure S9, HOMO and LUMO frontier orbital plots of the title complex on TD-DFT calculations; Figure S10, UV-Vis absorption spectra of complex, free ligand L and N719 recorded in $2x10^{-5}$ mol/L solution in ethanol; Figure S11,

cyclic voltammogram of $[Cu_2(L)_2dppm](PF_6)_2$ ($5x10^{-3}$ M) in acetonitrile at T = 298 K using NBu_4PF_6 (0.1 M) as supporting electrolyte (scan rate = 20 mVs^{-1}).

Author Contributions: C.A.-P., investigation, methodology, material analysis, and writing—original draft; J.J.C.-G., conceptualization, visualization, project administration, writing—original draft, and writing—review, and editing; E.A.R.-S., investigation, and methodology; A.C.-E., conceptualization, formal analysis, material analysis, and writing—original draft; R. S. -R., conceptualization, software and writing - original draft J.B.-L., conceptualization and software; J.JG, X-ray analysis, visualization, writing—original draft, writing—review and editing; M.F.-Á., X-ray and material analysis; V.M.-S., investigation, methodology; D.G.-M., software and validation. All authors have read and agreed to the published version of the manuscript.

Funding: This research received no external funding.

Institutional Review Board Statement: Not applicable

Informed Consent Statement: Not applicable

Data Availability Statement: Not applicable.

Acknowledgments: This work received financial support from Universidad Autónoma de Sinaloa, México (DGIP-PRO-A2-023) and from Consejo Nacional de Ciencia y Tecnología (CONACyT) in The form of a scholarship granted to C.A.-P (701513). The authors gratefully acknowledge access to the instrumental support in the USAII Facultad de Química. UNAM, México.

Conflicts of Interest: The authors declare no conflict of interest.

References

1. Caldeira, K.; Jain, A.K.; Hoffert, M.I. Climate Sensitivity Uncertainty and the Need for Energy Without CO2 Emission. *Science* **2003**, *299*, 2052–2054.
2. Olabi, A.G.; Abdelkareem, M.A. Renewable energy and climate change. *Renewable Sustainable Energy Rev.*, **2022**, *158*, 1-7.
3. Halkos, G.E.; Gkampoura, E.-C. Reviewing Usage, Potentials, and Limitations of Renewable Energy Sources. *Energies*, **2020**, *13*(11), 2906.
4. Eisenberg, R.; Nocera, D.G. Preface: Overview of the Forum on Solar and Renewable Energy. *Inorg. Chem*. **2005**, *44*, 6799–6801.
5. Cho, A. Energy's Tricky Tradeoffs. *Science* **2010**, *329*, 786–787.
6. Mauri, L.; Colombo, A.; Dragonetti, C.; Fagnani, F.A Fascinating Trip into Iron and Copper Dyes for DSSCs. *Inorganics* **2022**, *10*, 137.
7. O'Regan, B.; Grätzel. M. A Low-Cost, High-Efficiency Solar Cell Based on Dye-Sensitized Colloidal TiO2 Films. *Nature* **1991**, *353*, 737–740.
8. Solak, E. K.; Irmak, E. Advances in organic photovoltaic cells: a comprehensive review of materials, technologies, and performance. *RSC Adv.*, **2023**, *13*, 12244–12269.
9. Yahya, M.; Bouziani, A.; Ocak, C.; Seferoğlu, Z.; Sillanpää, M. Organic/metal ‐ organic photosensitizers for dye ‐ sensitized solar cells (DSSC): Recent developments, new trends, and future perceptions. *Dye. Pigment*. **2021**, *192*, 109227.
10. Housecroft, C.E.; Constable, E.C. Solar energy conversion using first-row d-block metal coordination compound sensitizers and redox mediators. *Chem. Sci*. **2022**, *13*, 1225 ‐ 1262.
11. Muñoz ‐ García, A.B.; Benesperi, I.; Boschloo, G.; Concepcion, J.J.; Delcamp, J.H.; Gibson, E.A.; Meyer, G.J.; Pavone, M.; Petters ‐ son, H.; Hagfeldt, A.; et al. Dye ‐ sensitized solar cells strike back. *Chem. Soc. Rev*. **2021**, *50*, 12450 ‐ 12550.
12. Hagfeldt, A.; Boschloo, G.; Sun, L.; Kloo, L.; Pettersson, H. Dye ‐ Sensitized Solar Cells. *Chem. Rev*. **2010**, *110*, 6595 ‐ 6663.
13. Polo, A.S.; Itokazu, M.K.; Iha, N.Y.M. Metal complex sensitizers in dye ‐ sensitized solar cells. *Chem. Rev*. **2004**, *248*, 1343 ‐ 1361.

14. Förster, C.; Heinze, K. Photophysics and photochemistry with Earth - abundant metals—Fundamentals and concepts. *Chem. Soc. Rev*. **2020**, *49*, 1057 – 1070.
15. Kokkonen, M.; Talebi, P.; Zhou, J.; Asgari, S.; Soomro, S.A.; Elsehrawy, F.; Halme, J.; Ahmad, S.; Hagfeldt, A.; Hashmi, S.G. Advanced research trends in dye - sensitized solar cells. *J. Mater. Chem. A* **2021**, *9*, 10527 – 10545.
16. Spinelli, G.; Freitag, M.; Benesperi, I. What is necessary to fill the technological gap to design sustainable dye-sensitized solar cells? *Sustainable Energy Fuels*, **2023**, *7*, 916-927.
17. Ozawa, H.; Sugiura, T.; Kuroda, T.; Nozawa, K.; Arakawa, H. Highly efficient dye-sensitized solar cells based on a ruthenium sensitizer bearing a hexylthiophene modified terpyridine ligand. *J. Mater. Chem. A*. **2016**, *4*, 1762-1770.
18. Mazloum-Ardakani, M.; Arazi, R. Improving the Effective Photovoltaic Performance in Dye-Sensitized Solar Cells Using an Azobenzenecarboxylic Acid-Based System. *Heliyon* **2019**, *5*, e01444.
19. J. Emsley, *The Elements*, Oxford University Press, Oxford, 3rd ed, 1998.
20. Risi, G.; Devereux, M.; Prescimone, A.; Housecroft, C.E.; Constable, E.C. Back to the future: asymmetrical D π A 2,2′ - bipyridine ligands for homoleptic copper(I)-based dyes in dye-sensitized solar cells. *RSC Adv*., **2023**, *13*, 4122 – 4137.
21. Beaudelot, J.; Oger, S.; Peruško, S.; Phan, T.-A.; Teunens, T.; Moucheron, C.; Evano G. Photoactive Copper Complexes: Properties and Applications. *Chem. Rev*., **2022**, *122*, 16365-16609.
22. Cao, Y.; Saygili, Y.; Ummadisingu, A.; Teuscher, J.; Luo, J.; Pellet, N.; Giordano, F.; Zakeeruddin, S.M.; Moser, J. - E.; Freitag, M.; Hagfeldt, A.; Grätzel, M. 11% efficiency solid - state dye - sensitized solar cells with copper(II/I) hole transport materials. *Nat. Commun*. **2017**, *8*, 15390.
23. Colombo, A.; Dragonetti, C.; Roberto, D.; Fagnani, F. Copper Complexes as Alternative Redox Mediators in Dye - Sensitized Solar Cells. *Molecules* **2021**, *26*, 194.
24. Franchi, D.; Leandri, V.; Pia Pizzichetti, A.R.; Xu, B.; Hao, Y.; Zhang, W.; Sloboda, T.; Svanström, S.; Cappel, U.B.; Kloo, L.; Sun, L.; Gardner, J.M. Effect of the Ancillary Ligand on the Performance of Heteroleptic Cu(I) Diimine Complexes as Dyes in Dye - Sensitized Solar Cells. *ACS Appl. Energy Mater*. **2022**, *5*, 1460−1470.
25. Alonso-Vante, N.; Nierengarten, J.F.; Sauvage, J.P. Spectral sensitization of large-band-gap semiconductors (thin films and ceramics) by a carboxylated bis(1,10-phenanthroline)copper(I) complex. *J. Chem. Soc., Dalton Trans*., **1994**, 1649 -1654.
26. Karpacheva, M.; Malzner, F.J.; Wobill, C.; Büttner, A.; Constable, E.C.; Housecroft, C.E. Cuprophilia: Dye-Sensitized Solar Cells with Copper(I) Dyes and Copper(I)/(II) Redox Shuttles. *Dyes Pigment*. **2018**, *156*, 410–416.
27. Lennert, A.; Guldi, D.M. Homoleptic and Heteroleptic Copper Complexes as Redox Couples in Dye-Sensitized Solar Cells. *ChemPhotoChem* **2019**, *3*, 636–644.
28. Conradie, J. Polypyridyl copper complexes as dye sensitizer and redox mediator for dye-sensitized solar cells. *Electrochemistry Communications*, **2022**, *134*, 107182.
29. Báez - Castro, A.; Baldenebro - López, J.; Cruz - Enríquez, A.; Höpfl, H.; Glossman - Mitnik, D.; Miranda - Soto, V.; Parra - Hake, M.; Reynoso - Soto, E.; Campos - Gaxiola, J.J. Heteroleptic Cu(I) complexes containing polypyridyl ligands and triphenylphosphine: Synthesis, structure, photophysical properties, DFT studies and applications in co - sensitized solar cells. *Inorg. Chim. Acta* **2017**, *466*, 486 – 496.
30. Soto-Acosta, M.; Campos - Gaxiola, J.J.; Reynoso - Soto, E.; Cruz - Enríquez, A.; Baldenebro - López, J.; Höpfl, H.; García, J.J.; Flores-Álamo, M.; Miranda - Soto, V.; Glossman - Mitnik, D. Synthesis, Crystal Structure, DFT Studies and Optical/Electrochemical Properties of Two Novel Heteroleptic Copper(I) Complexes and Application in DSSC. *Crystals* **2022**, 12, 1240.
31. Andrés - Tomé, I.; Fyson, J.; Dias, F.B.; Monkman, A.P.; Iacobellis, G.; Coppo, P. Copper(i) complexes with bipyridyl and phosphine ligands: A systematic study. *Dalton Trans*. **2012**, *41*, 8669 – 8674.
32. Pavia, D.; Lampman, G.; Kriz, G.; Vyvyan, J. *Introduction to Spectroscopy*; Cengage Learning: Belmont, CA, USA, 2008.
33. Báez - Castro, A.; Baldenebro - López, J.; Cruz - Enríquez, A.; Höpfl, H.; Glossman - Mitnik, D.; Valentín, M. - S.; Parra - Hake, M.; Campos - Gaxiola, J.J. Synthesis, structure, characterization and photophysical properties of copper(i) complexes containing polypyridyl ligands. *RSC Adv*. **2014**, 4, 42624–42631.
34. Gusev, A.; Kiskin, M.; Braga, E.; Zamnius, E.; Kryukova, M.; Karaush-Karmazin, N.; Baryshnikov, G.; Minaev, B.; Linert, W. Structure and emission properties of dinuclear copper(I) complexes with pyridyltriazole. *RSC Adv*., **2023**, *13*, 3899–3909.

35. Yang, L.; Powell, D.R.; Houser, R.P. Structural variation in copper(i) complexes with pyridylmethylamide ligands: Structural analysis with a new four - coordinate geometry index, τ4. *Dalton Trans*. **2007**, 955 – 964.
36. Femoni, C.; Muzzioli, S.; Palazzi, A.; Stagni, S.; Zacchini, S.; Monti, F.; Accorsi, G.; Bolognesi, M.; Armaroli, N.; Massi, M.; Valenti, G.; Marcaccio, M. New tetrazole-based Cu(I) homo- and heteroleptic complexes with various P^P ligands: synthesis, characterization, redox and photophysical properties. *Dalton Trans*., **2013**, *42*, 997–1010.
37. Tong, Y.; Chen, X. -W.; He, L.-H.; Chen, J.-L.; Liu, S.-J.; Wen, H.-R. Reversible stimuli-responsive luminescence of bimetallic cuprous complexes based on NH-deprotonated 3-(2′ -pyridyl)pyrazole. *J. Mater. Chem. C*, **2021**, 9, 16664-16671.
38. Pathaw, L.; Khamrang, T.; Kathiravan, A.; Velusamy, M. Synthesis, crystal structure, bovine serum albumin binding studies of 1,2,4-triazine based copper(I) complexes. *J. Mol. Struct*. **2020**, *1207*, 127821.
39. Janiak, C. A critical account on π–π stacking in metal complexes with aromatic nitrogen-containing ligands. *J. Chem. Soc., Dalton Trans*. **2000**, 3885.
40. Wöhler, J.; Meyer, M.; Prescimone, A.; Housecrof, C.E.; Constable, E.C. The effects of introducing terminal alkenyl substituents into the 2,2′-bipyridine domain in [Cu(N^N)(P^P)]+ coordination compounds. *Dalton Trans*., **2022**,*51*, 13094-13105.
41. Nishio, M.; Umezawa, Y.; Honda, K.; Tsuboyama, S.; Suezawa, H. CH/π hydrogen bonds in organic and organometallic chemistry. *CrystEngComm*, **2009**, *11*, 1757—1788.
42. Keller, S.; Prescimone, A.; Constable, E.C.; Housecroft, C.E. Dinuclear [Cu2(N^N)(P^P)2][PF6]2 complexes containing bridging 2,3,5,6-tetra(pyridin-2-yl)pyrazine or 2,4,6-tri(pyridin-2-yl)-1,3,5-triazine ligands. *Polyhedron* **2016**, *116*, 3-11.
43. Báez - Castro, A.; Baldenebro - López, J.; Ceballos - Mendivil, L.; Román - Bravo, P.P.; Höpfl, H.; Miranda - Soto, V.; Glossman - Mitnik, D.; Cruz - Enríquez, A.; Campos - Gaxiola, J.J. Synthesis, crystal structure, DFT studies and photophysical properties of a copper(I) – triphenylphosphane complex based on trans - (±) - 2,4,5 - tris - (pyridin - 2 - yl) - 2 - imidazoline. *Acta Crystallogr. C Struct. Chem*. **2017**, *73*, 280 – 286.
44. Spackman, M.A.; Jayatilaka, D. Hirshfeld surface analysis. *CrystEngComm*. **2009**, *11*, 19–32.
45. Tan, S.L.; Jotani, M.M.; Tiekink, E. R. T. Utilizing Hirshfeld surface calculations, non-covalent interaction (NCI) plots and the calculation of interaction energies in the análisis of molecular packing. *Acta Cryst*. **2019**, *E75*, 308–318.
46. McKinnon, J.J.; Jayatilaka, D.; Spackman, M.A. Towards quantitative analysis of intermolecular interactions with Hirshfeld surfaces. *Chem. Commun*. **2007**, 3814-3816.
47. Spackman, M.A.; McKinnon, J.J. Fingerprinting intermolecular interactions in molecular crystals. *CrystEngComm*. **2002**, *4*, 378-392.
48. McKinnon, J.J.; Spackman, M.A.; Mitchell, A.S. Novel tools for visualizing and exploring intermolecular interactions in molecular crystals. *Acta Crystallogr. Sect. B Struct. Sci*. **2004**, *B60*, 627 – 668.
49. Hohenberg, P.; Kohn, W. Inhomogeneous Electron Gas. *Phys. Rev*. **1964**, *136*, B864–B871.
50. Kohn, W.; Sham, L.J. Self - consistent equations including exchange and correlation effects. *Phys. Rev.* **1965**, *140*, A1133 – A1138.
51. Stratmann, R.E.; Scuseria, G.E.; Frisch, M.J. An efficient implementation of time - dependent density - functional theory for the calculation of excitation energies of large molecules. *J. Chem. Phys*. **1998**, *109*, 8218 – 8224.
52. Burke, K.; Werschnik, J.; Gross, E. Time - dependent density functional theory: Past, present, and future. *J. Chem. Phys.* **2005**, *123*, 062206.
53. Zhao, Y.; Truhlar, D.G. The M06 suite of density functionals for main group thermochemistry, thermochemical kinetics, non - covalent interactions, excited states, and transition elements: Two new functionals and systematic testing of four M06 - class functionals and 12 other functionals. *Theor. Chem. Acc.* **2008**, *120*, 215–241.
54. Rassolov, V.A.; Ratner, M.A.; Pople, J.A.; Redfern, P.C.; Curtiss, L.A. 6 - 31G* basis set for third - row atoms. *J. Comput. Chem.* **2001**, *22*, 976 – 984.
55. Sosa, C.; Andzelm, J.; Elkin, B.C.; Wimmer, E.; Dobbs, K.D.; Dixon, D.A. A local density functional study of the structure and vibrational frequencies of molecular transition - metal compounds. *J. Phys. Chem*. **1992**, *96*, 6630 – 6636.
56. Wei, L.; Yang, Y.; Fan, R.; Na, Y.; Wang, P.; Dong, Y.; Yang, B.; Cao, W. N,N′-Bis((6-methoxylpyridin-2-yl)methylene)- p-phenylenediimine based d^{10} transition metal complexes and their utilization in co-sensitized solar cells. *Dalton Trans.*, **2014**, *43*, 11361–11370.

57. Gao, S.; Fan, R.Q.; Wang, X.M.; Qiang, L.S.; Wei, L.G.; Wang, P.; Yang, Y.L.; Yu Lei Wang, Y.L.; Luan, T.Z. Multifunctional Zn(II)/Cd(II) metal complexes for tunable luminescence properties and highly efficient dye - sensitized solar cells. *RSC Adv*. **2015**, *5*, 43705–43716.
58. Baranova, K.F.; Titov, A.A.; Smol'yakov, A.; Chernyadyev, A.; Filippov, O.A.; Shubina, E. Mononuclear Copper(I) 3-(2-pyridyl)pyrazole Complexes: The Crucial Role of Phosphine on Photoluminescence. *Molecules* **2021**, *26*(22), 6869.
59. Li, C.; Li, W.; Henwood, A.F.; Hall, D.; Cordes, B.D.; Slawin, A.M.Z.; Lemaur, V.; Olivier, Y.; Samuel, I.D.W.; Zysman-Colman, E. Luminescent Dinuclear Copper(I) Complexes Bearing an Imidazolylpyrimidine Bridging Ligand. *Inorg. Chem*. **2020**, *59*, 20, 14772–14784.
60. Peppas, A.; Sokalis, D.; Perganti, D.; Schnakenburg, G.; Falaras, P.; Philippopoulos, A.I. Sterically demanding pyridine-quinoline anchoring ligands as building blocks for copper(I)-based dye-sensitized solar cell (DSSC) complexes. *Dalton Trans*., **2022**, *51*, 15049–15066.
61. Kumar, A.; Vashistha, V.K.; Tevatia, P.; Singh, R. Voltammetric Determination of Molecular Modeling Parameters for Pen - taazamacrocyclic Complexes of Mn(II) and Co(II). *Anal. Bioanal. Electrochem*. **2016**, *8*, 848 - 861.
62. Al-horaibi, S.A.; Asiri, A.M.; El-Shishtawy, R.M.; Gaikwad, S.T.; Rajbhoj, A.S. Indoline, and benzothiazole-based squaraine dye-sensitized solar cells containing bis-pendent sulfonate groups: Synthesis, characterization and solar cell performance. *J. Mol. Struct*. **2019**, *1195*, 591-597.
63. Portillo - Cortez, K.; Martínez, A.; Dutt, A.; Santana, G. N719 Derivatives for Application in a Dye - Sensitized Solar Cell (DSSC): A Theoretical Study. *J. Phys. Chem. A* **2019**, *123*, 10930 - 10939.
64. *CrysAlisPro*, Version 1.171.37.35; Agilent Technologies: Yarnton, UK, 2014.
65. Clark, R.C.; Reid, J.S. The analytical calculation of absorption in multifaceted crystals. *Acta Crystallogr. Sect. A* Found. Crystallogr.**1995**, *A51*, 887–897.
66. Sheldrick, G.M. ShelXT - Integrated space - group and crystal - structure determination. *Acta Cryst.* **2015**, A71, 3 - 8.
67. Sheldrick, G.M. Crystal structure refinement with SHELXL. *Acta Crystallogr. Sect. C Struct. Chem*. **2015**, *C71*, 3–8.
68. Macrae, C.F.; Bruno, I.J.; Chisholm, J.A.; Edgington, P.R.; McCabe, P.; Pidcock, E.; Rodriguez - Monge, L.; Taylor, R.; van de Streek, J.; Wood, P.A. Mercury CSD 2.0—New features for the visualization and investigation of crystal structures. *J. Appl. Crystallogr*. **2008**, *41*, 466–470.
69. Brandenburg, K. *Diamond*, version 4.3.2; Crystal Impact GbR: Bonn, Germany, 2017.
70. Ito, S.; Chen, P.; Comte, P.; Nazeeruddin, M.K.; Liska, P.; Péchy, P.; Grätzel, M. Fabrication of screen-printing pastes from TiO_2 powders for dye-sensitized solar cells Prog. *Photovoltaics*, **2007**, *15*, 603-612.
71. Ito, S.; Murakami, T.N.; Comte, P.; Liska, P.; C. Grätzel, C.; Nazeeruddin, M.K.; Grätzel, M. Fabrication of Thin Film Dye Sensitized Solar Cells with Solar to Electric Power Conversion Efficiency over 10%. *Thin Solid Films*, **2008**, *516*, 4613-4619.
72. Turner, M.J.; McKinnon, J.J.; Wolff, S.K.; Grimwood, D.J.; Spackman, P.R.; Jayatilaka, D.; Spackman, M.A. *CrystalExplorer17*; University of Western Australia: Crawley, WA, Australia, 2017.
73. Frisch, M.J.; Trucks, G.W.; Schlegel, H.B.; Scuseria, G.E.; Robb, M.A.; Cheeseman, J.R.; Scalmani, G.; Mennucci, V.B.; Petersson, G.A.; Nakatsuji, H. et al. *Gaussian 09*, Revision A. 02; Gaussian Inc.: Wallingford, CT, USA, 2009.
74. Dennington, R.; Keith, T.; Millam, J.; Eppinnett, K.; Hovell, W.L.; Gilliland, R. *GaussView*, version 5.0.9; Semichem, Inc.: Shawnee Mission, KS, USA, 2009.
75. Gorelsky, S.I.; Lever, A.B.P. Electronic Structure and Spectra of Ruthenium Diimine Complexes by Density Functional Theory and INDO/S. Comparison of the Two Methods. *J. Organomet. Chem.* **2001**, *635*, 187–196.
76. Scrocco, E.; Tomasi, J. Electronic Molecular Structure, Reactivity and Intermolecular Forces: An Euristic Interpretation by Means of Electrostatic Molecular Potentials. *Adv. Quantum Chem*. **1978**, *11*, 115–193.
77. Improta, R.; Barone, V.; Scalmani, G.; Frisch, M.J. A State-Specific Polarizable Continuum Model Time-Dependent Density Functional Theory Method for Excited State Calculations in Solution. *J. Chem. Phys*. **2006**, *125*, 054103.